

Partial cation ordering, relaxor ferroelectricity, and ferrimagnetism in $\text{Pb}(\text{Fe}_{1-x}\text{Yb}_x)_{2/3}\text{W}_{1/3}\text{O}_3$ solid solutions

Cite as: J. Appl. Phys. **128**, 134102 (2020); <https://doi.org/10.1063/5.0011576>

Submitted: 22 April 2020 . Accepted: 18 September 2020 . Published Online: 06 October 2020

S. A. Ivanov, D. C. Joshi, A. A. Bush , D. Wang, B. Sanyal , O. Eriksson, P. Nordblad , and R. Mathieu 



ARTICLES YOU MAY BE INTERESTED IN

Coexistence of two ferroelectric phases and improved room-temperature multiferroic properties in the $(0.70)\text{BiFe}_{1-x}\text{Co}_x\text{O}_3-(0.30)\text{PbTiO}_3$ system

Journal of Applied Physics **128**, 124102 (2020); <https://doi.org/10.1063/5.0019764>

Effect of ferroelectric domain walls on the dielectric properties of PbZrO_3 thin films

Applied Physics Letters **117**, 142905 (2020); <https://doi.org/10.1063/5.0017984>

Correlations between first-principles calculations and electric properties of $\text{HfO}_2:\text{Al}_2\text{O}_3$ alloys for metal-insulator-metal (MIM) capacitor applications

Journal of Applied Physics **128**, 134101 (2020); <https://doi.org/10.1063/5.0025130>

Meet the Next Generation
of Quantum Analyzers

And Join the Launch
Event on November 17th



Register now



Partial cation ordering, relaxor ferroelectricity, and ferrimagnetism in $\text{Pb}(\text{Fe}_{1-x}\text{Yb}_x)_{2/3}\text{W}_{1/3}\text{O}_3$ solid solutions

Cite as: J. Appl. Phys. 128, 134102 (2020); doi: 10.1063/5.0011576

Submitted: 22 April 2020 · Accepted: 18 September 2020 ·

Published Online: 6 October 2020



S. A. Ivanov,^{1,2} D. C. Joshi,² A. A. Bush,³ D. Wang,⁴ B. Sanyal,⁴ O. Eriksson,⁴ P. Nordblad,²
and R. Mathieu^{2,a)}

AFFILIATIONS

¹Department of Chemistry, M.V. Lomonosov Moscow State University, Leninskie Gory 1/3, Moscow 119991, Russia

²Department of Materials Science and Engineering, Uppsala University, Box 35, SE-751 03 Uppsala, Sweden

³MIREA—Russian Technological University (RTU MIREA), Moscow 119454, Russia

⁴Department of Physics and Astronomy, Uppsala University, Box 516, 751 20 Uppsala, Sweden

^{a)}Author to whom correspondence should be addressed: roland.mathieu@angstrom.uu.se

ABSTRACT

The structural, magnetic, and dielectric properties of ceramic samples of Yb-doped $\text{PbFe}_{2/3}\text{W}_{1/3}\text{O}_3$ have been investigated by a variety of methods including x-ray powder diffraction, magnetometry, and dielectric spectroscopy. In addition, theoretical investigations were made using first-principles density functional calculations. All the doped samples $\text{Pb}(\text{Fe}_{1-x}\text{Yb}_x)_{2/3}\text{W}_{1/3}\text{O}_3$ (PFYWO) ($0.1 \leq x \leq 0.5$) were found to crystallize in an ordered cubic ($Fm\bar{3}m$) structure with partial ordering in the B-perovskite sites. Observed changes in the cationic order were accompanied by differences in the dielectric and magnetic responses of the system. While pure $\text{PbFe}_{2/3}\text{W}_{1/3}\text{O}_3$ is antiferromagnetic, the doped $\text{Pb}(\text{Fe}_{1-x}\text{Yb}_x)_{2/3}\text{W}_{1/3}\text{O}_3$ PFYWO samples display excess moments and ferrimagnetic-like behavior, associated with differences in B' and B'' site occupancies of the magnetic Fe^{3+} cations. The magnetic transition temperature of the ferrimagnetic phase is found to decrease with increasing Yb content, from $T_N \sim 350$ K of the undoped sample down to 137 K for $x = 0.5$. All PFYWO compounds display a ferroelectric relaxor behavior akin to that of $\text{PbFe}_{2/3}\text{W}_{1/3}\text{O}_3$, albeit our results show significant changes of the frequency and temperature dependence of the dielectric properties. The changes of the properties of PFYWO with increasing Yb substitution can be explained by the changes in the cation size/charge mismatch and the size difference of the two ordered positions.

© 2020 Author(s). All article content, except where otherwise noted, is licensed under a Creative Commons Attribution (CC BY) license (<http://creativecommons.org/licenses/by/4.0/>). <https://doi.org/10.1063/5.0011576>

INTRODUCTION

Studies of dielectric and magnetic properties of Pb-based perovskites have revealed several new multiferroic (MF) materials.^{1–7} The consequences and cause of cationic order on the B-site in such perovskites have been discussed in the literature.^{8–10} Ionization potentials, cation coordination geometry, and the A-cation/B-cation size ratio are factors that influence the degree of ordering.¹¹ $\text{PbFe}_{2/3}\text{W}_{1/3}\text{O}_3$ (PFWO) was the first reported MF material in the double perovskite family $\text{PbB}_{2/3}^3\text{B}_{1/3}^6\text{O}_3$.¹² The initial idea behind the preparation of PFWO was based on the search for ferrimagnetic perovskites with some kind of order of the B-site cations creating two sublattices corresponding to the

formula $\text{Pb}[\text{Fe}]_{0.5}[\text{Fe}_{1/3}\text{W}_{2/3}]_{0.5}\text{O}_3$. In this case, the magnetic moments of two sublattices directed oppositely to each other are not compensated, and the ferroelectric material also becomes ferrimagnetic. Some experimental results indicate that partial order may occur and that the structural formula for PFWO could be written $\text{Pb}[\text{Fe}_{1-y}\text{W}_y]_{0.5}[\text{Fe}_{1/3+y}\text{W}_{2/3-y}]_{0.5}\text{O}_3$ with $0 \leq y \leq 1/3$.¹² However, it has been found impossible to realize substantial cationic order in undoped PFWO.

PFWO is a Pb-based 2:1 perovskite that combines magnetically active Fe^{3+} cations and ferroelectrically active W^{6+} cations.^{13,14} PFWO orders antiferromagnetically at about 350 K and shows relaxor ferroelectric behavior between 150 and 200 K. In the last

few years, several attempts have been made to modify the properties of PFWO by substitutions at the *A* or (and) *B* crystallographic sites. Results from studies using various solid solutions have been reported, for instance, by *A*-site doping^{15–17} and *B*-site substitution.^{18–23} These studies show that the magnetic and dielectric properties of PFWO can be modified and controlled by cation substitution.

Although major advances have been made in optimizing PFWO for a variety of applications, several fundamental aspects of their behavior, in particular, the nature of the compositional and spin ordering and its relation to the relaxor properties remain unresolved.^{24–27}

The aim of the present work is to clarify the effect of substitution of Yb^{3+} for Fe^{3+} on the structural, magnetic, and dielectric properties of PFWO. The selection of Yb^{3+} substitution is related to its large cation size and small electronegativity providing optimal conditions to create cation ordering and polar bonds. We have prepared phase-pure, stoichiometric $\text{Pb}(\text{Fe}_{1-x}\text{Yb}_x)_{2/3}\text{W}_{1/3}\text{O}_3$ (PFYWO) samples of composition $x = 0, 0.1, 0.2, 0.3, 0.4$, and 0.5 and investigate these by x-ray powder diffraction, magnetometry, dielectric spectroscopy, and electron microscopy. The Yb doping is found to promote cationic ordering of the Fe(Yb) and W cations on the *B* site. The experiments are accompanied by theoretical studies of magnetic interactions for several key Yb concentrations using first-principles calculations.

METHODS

$\text{Pb}(\text{Fe}_{1-x}\text{Yb}_x)_{2/3}\text{W}_{1/3}\text{O}_3$ ($0 \leq x \leq 0.5$) samples were synthesized as ceramics by a conventional multiple-step solid state reaction method in the air;¹⁸ see the [supplementary material](#) for more details about the synthesis and the characterization methods. Chemical composition was checked using scanning electron microscopy (SEM) images, x-ray energy dispersive spectroscopy (EDS), and inductively coupled plasma (ICP) analyses. X-ray powder diffraction (XRPD) was used for both phase analysis and advanced Rietveld analyses using the FULLPROF program.²⁸ The (magneto)dielectric measurements were performed using a LCR meter and a customized PPMS probe, while magnetic measurements were collected using a superconducting quantum interference device (SQUID) magnetometer from Quantum Design Inc.

We have performed first-principles density functional calculations to study the energetics and structural and magnetic properties of PFYWO, employing the VASP package.^{29,30} Perdew–Burke–Ernzerhof³¹ generalized gradient approximation (GGA) has been considered for the treatment of exchange–correlation functional. Strong electron correlations in the d-orbitals have been included in a static mean-field approach (GGA + U).^{32,33} We have considered the U_{eff} ($U - J$ where U is the Coulomb parameter and J is the Hund parameter) value of 4 eV for the Fe-d electrons;³⁴ see the [supplementary material](#) for more information.

RESULTS

XRPD studies

The SEM images indicate that as in, e.g., the doping of PFWO by Mn or Sc,^{18,22} the average grain size ($\sim 2\text{--}6\mu\text{m}$ for undoped PFWO) is slightly decreasing as the doping of Yb increases (see

Fig. SM1 in the [supplementary material](#)). The PFYWO ceramics have 90%–93% of the theoretical density values. EDS analyses evidence close to nominal stoichiometry of Pb, Fe, Yb, and W cations (see Table SM1 in the [supplementary material](#)). Room temperature XRPD patterns of the PFYWO ($0 \leq x \leq 0.5$) samples are shown in Fig. 1. The position and intensities of the reflections in the XRPD patterns of the samples were consistent with those expected for PFWO-based solid solutions with the cubic perovskite structure.¹⁸ Reflections from secondary phases were not detected. Structural refinements of the XRPD powder diffraction patterns of PFYWO with $x < 0.1$ confirm that these samples stabilize in the cubic $Pm\bar{3}m$ symmetry at room temperature. For samples with $0.1 \leq x \leq 0.5$, a set of additional superstructure reflections were found [e.g., (111) at around 19° in addition to the Bragg (200) at around 22° , the x -dependences of which are illustrated in Fig. 2] and the crystal structure of PFYWO ($x \geq 0.1$) stabilizes in the cubic $Fm\bar{3}m$ symmetry. Thus, the addition of few percent of Yb to PFWO leads to *B*-site cation ordering (introduction of two independent *B*-sites). The evolution of the lattice parameter (a) for the different samples is plotted in Fig. 3(a), and there is a continuous increase of a with increasing Yb content. This increase is in accord with the size difference between Yb^{3+} (0.868 Å) and Fe^{3+} (0.645 Å) cations for coordination number 6.³⁶

The structural refinements of XRPD patterns measured on the $x = 0.1, 0.2, 0.3, 0.4$, and 0.5 samples [Figs. 1(b)–1(f)] were performed in the $Fm\bar{3}m$ space group (No. 225). The Fe, Yb, and W atoms are located at the $4a$ (0,0,0) and $4b$ (0.5,0.5,0.5) crystallographic Wyckoff sites [which we refer to as $B(4a)$ and $B(4b)$ in the following]. The O atoms are found at the $24e$ site ($x,0,0$) for an ideal primitive cubic cell and its deviation from 0.25 determines the difference between $B(4a)$ –O and $B(4b)$ –O distances. Finally, the Pb atoms occupy the $32f$ (y,y,y) sites, presenting an off-center displacement along the $[111]$ direction. The $Fm\bar{3}m$ space group does not allow any tilt nor rotation of the BO_6 coordination octahedra nor polyhedral distortions; however, different B–O bond distances are permitted owing to the presence of partial cation ordering. The refined B–O bond lengths are indeed different and their x -dependence plotted in Fig. 3(b).

The distribution of the three different transition metal cations on the two available *B* sites and the Pb and O stoichiometry have been refined assuming the nominal Fe:Yb:W ratio and using the determined ratio of (Fe + Yb)/W on the two sites from the refinement of XRPD data. Due to their different scattering form, factors Fe^{3+} and Yb^{3+} are well distinguishable in x-ray scattering. The refinements indicate an increase of the degree of cation site order as the Yb content increases. Normally,^{18,37} determination of the distribution of three different kinds of atoms (Fe, Yb, and W) on two available crystallographic sites ($4a$ and $4b$ in $Fm\bar{3}m$) requires at least two sets of diffraction data with differing atomic cross sections. However, using only XRPD data and the nominal composition in the refinements, conclusive results about the cation distribution were achieved. The resulting cation distributions on the $4a$ and $4b$ sites are presented in Fig. 4. Polyhedral analysis was made by the IVTON software, and the results are presented in Table SM3 in the [supplementary material](#). The oxidation states of the cations, determined by bond valence calculations, are consistent with Pb^{2+} , Fe^{3+} , Yb^{3+} , and W^{6+} (see Table SM1 in the [supplementary material](#)).

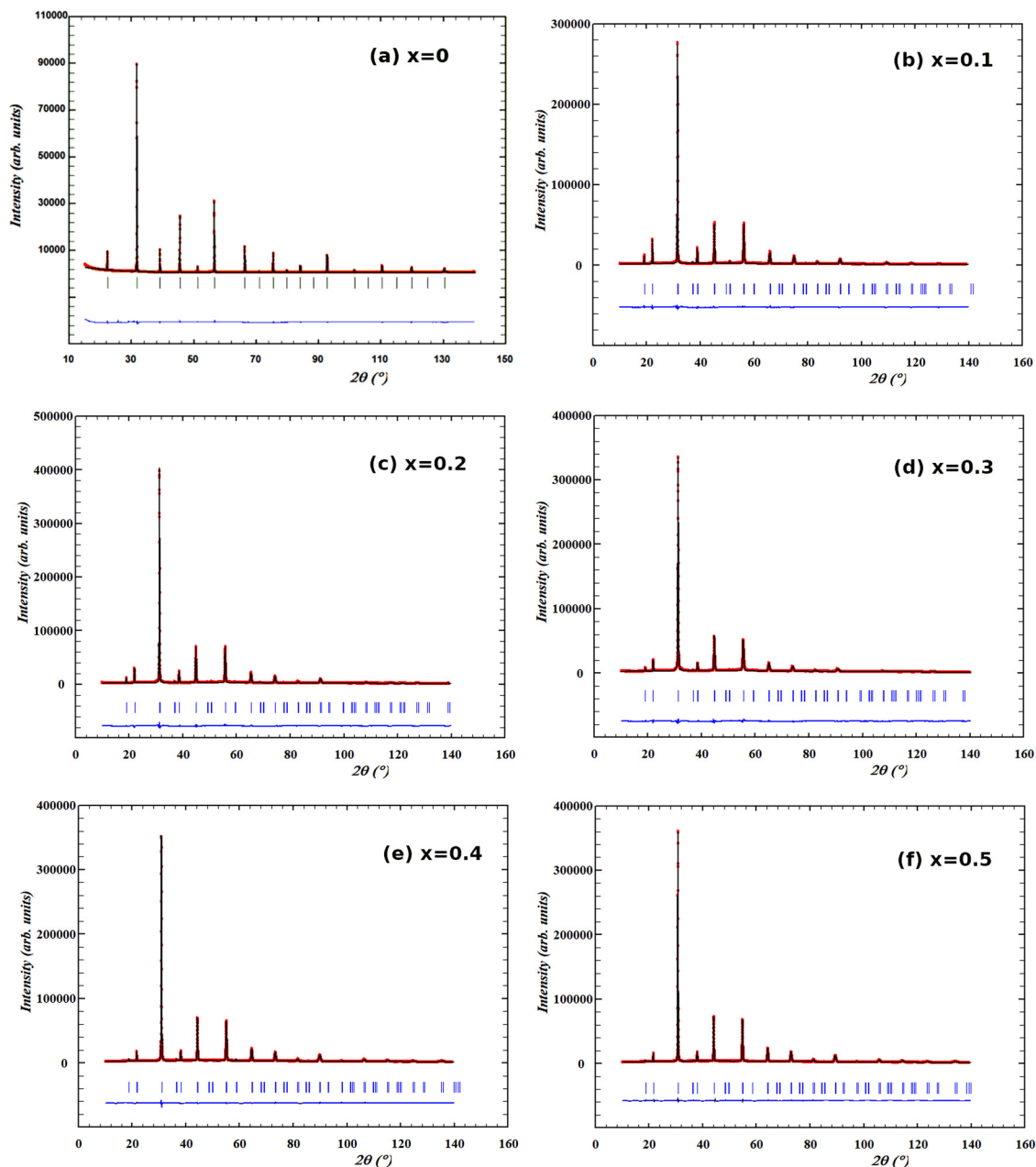


FIG. 1. X-ray powder diffraction patterns for polycrystalline $\text{Pb}(\text{Fe}_{1-x}\text{Yb}_x)_{2/3}\text{W}_{1/3}\text{O}_3$ for $0 \leq x \leq 0.5$ together with their Rietveld refinements. $x =$ (a) 0, (b) 0.1, (c) 0.2, (d) 0.3, (e) 0.4, and (f) 0.5; see Table SM2 in the [supplementary material](#) for quality R-factors and goodness of fit values.

Theoretical results

Our experimental results indicate that Yb replaces Fe in the *B* sublattice with W sites remaining almost unaffected. For this reason, Fe atoms have been substituted solely by Yb atoms in our calculations. Two concentrations of Yb were considered initially with two different configurations to check whether the Yb atoms

are more likely to be periodically distributed in the structure for high Yb concentrations. We built structural models with the periodic and clustered arrangement of Yb atoms for two different concentrations: $x = 0.25$ and $x = 0.375$. The supercells were built up with six octahedra along the *c* axis and $\sqrt{2}a \times \sqrt{2}a$ in-plane geometry. In [Table I](#), we show the relative energies of FM and

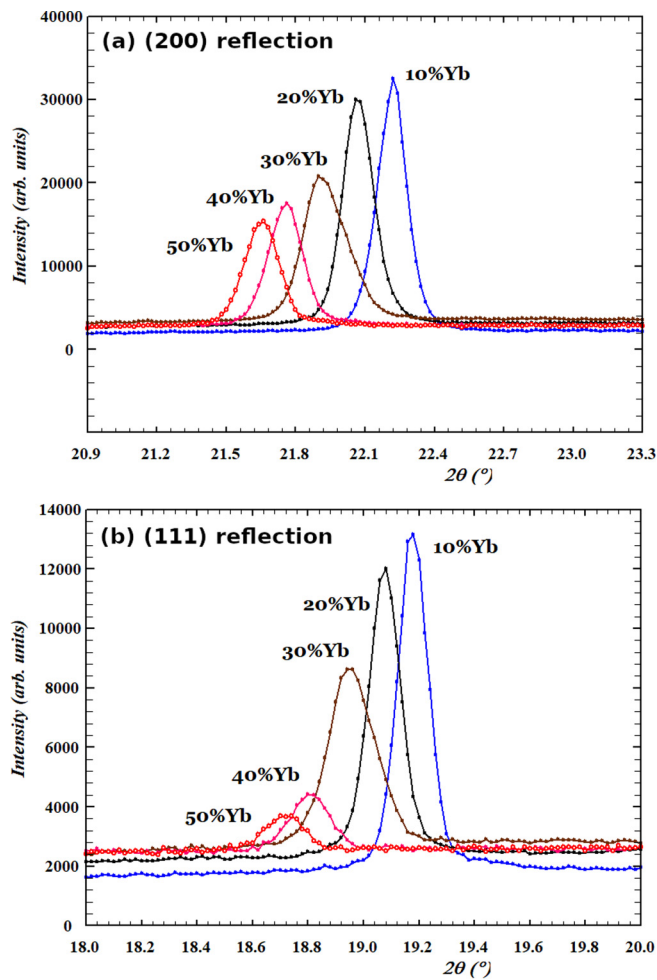


FIG. 2. (a) (200) Bragg reflections and (b) (111) superlattice reflection for $\text{Pb}(\text{Fe}_{1-x}\text{Yb}_x)_{2/3}\text{W}_{1/3}\text{O}_3$ ($0.1 \leq x \leq 0.5$).

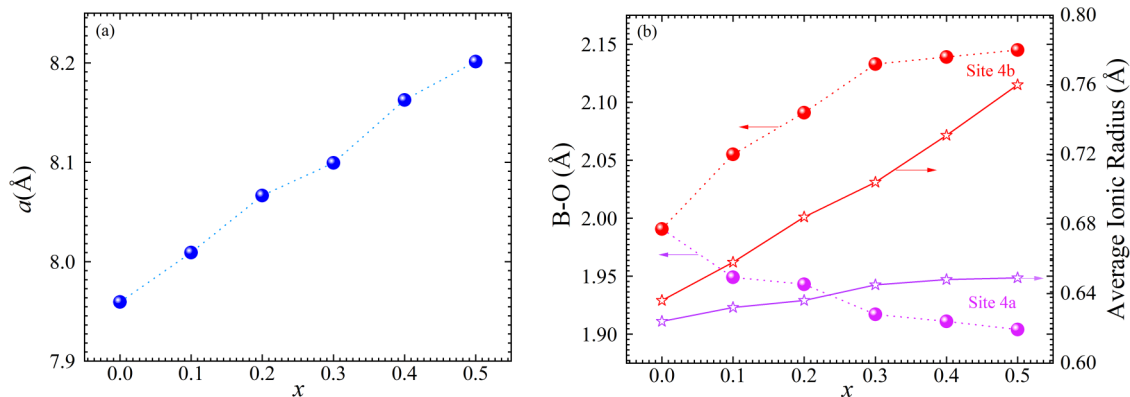


FIG. 3. Compositional dependence of (a) lattice parameter and (b) bond length $B-O$ for 4a and 4b sites; the theoretical average ionic radius is added in panel (b) for comparison. In order to compare these data with the lattice parameter of ordered $Fm\bar{3}m$ samples, we have doubled the lattice parameter of the compound with $x = 0$.

AFM alignments of Fe moments. First, we note that structures with periodic arrangement always have lower energy than the clustered structure. The energy difference between periodic and non-periodic distribution increases as the concentration increases (from 12.33 meV/atom to 16.50 meV/atom). Second, AFM configurations are always energetically more favorable than the FM configurations. In addition, if we only focus on the ground state configuration, i.e., periodic arrangement of Yb, as the Yb concentration increases, the energy difference between AFM and FM decreases (from 11.17 meV/atom to 2.17 meV/atom). This is because Fe atoms on the average are situated more distantly, and hence the strength of exchange interaction decreases.

For simulating a lower concentration, we built another supercell with six octahedra along the c axis and $2\sqrt{2}a \times 2\sqrt{2}a$ in-plane geometry. In this case, we performed calculations for the lowest concentration, $x = 0.125$, in the supercell containing 240 atoms. We have also simulated the highest concentration ($x = 0.375$) with the supercell containing 240 atoms to check the consistency of results obtained with the supercell containing 60 atoms. Figure 5 is an example of the structure we used for the simulation. The results are shown in Table II. At high Yb concentration, the lowest energy state occurs for the periodic structure with the AFM configuration, and the second-lowest energy state is the random structure with the AFM configuration; the energy difference between these two states being 9.75 meV/atom. On the contrary, at low Yb concentration, the ground state turns out to be a randomly distributed structure where the energies of the periodic and clustered structures are 2.38 meV/atom and 3.71 meV/atom higher than the ground state, respectively. According to our simulation, as the Yb concentration increases, we expect a transition from a randomly distributed phase to a periodically distributed phase. We also compared the average magnetic moment of Fe for different Yb doping and the average volume of the octahedra before and after doping. The results are shown in Tables III and IV. It has been observed that the volume of PFWO increases after Yb doping. It is also seen that the FeO_6 octahedra are modified more significantly than the WO_6 octahedra. Besides that, according to the histograms of the optimized bond lengths shown in Fig. 6, we can conclude that a significant variation

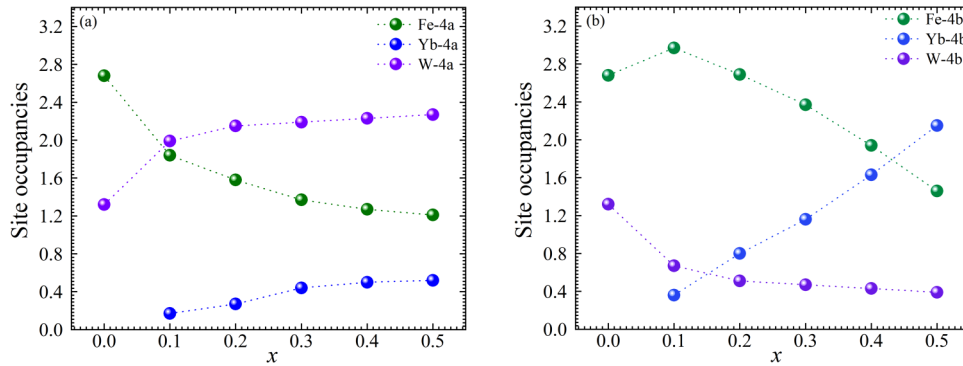


FIG. 4. Compositional dependence of site occupancies for Fe, Yb, and W for (a) 4a site and (b) 4b site determined from the XRPD data.

TABLE I. The result from calculations with 60 atoms structures, relative energies, unit in meV/atom.

x	Periodic		Cluster	
	FM	AFM	FM	AFM
0.250	11.17	0.00	22.00	12.33
0.375	2.17	0.00	27.67	16.50

exists among the species. It is found that most of the Pb–Fe bond lengths are smaller than the average Pb–B bond length, while Pb–W bond lengths are bigger. The corresponding Fe–O–Fe bond angle distribution is shown in Fig. SM2 in the [supplementary material](#), angles ranging from 158° to 175° . According to the Goodenough–Kanamori rule, when the bond angle is close to 180° , the Fe–O–Fe bond with d^5 – d^5 interacting cations shows AFM superexchange interaction. One can clearly see that for $x = 0.125$, there are more Fe–O–Fe networks, and more importantly most of the bond angles are close to 180° giving rise to stronger AFM superexchange.

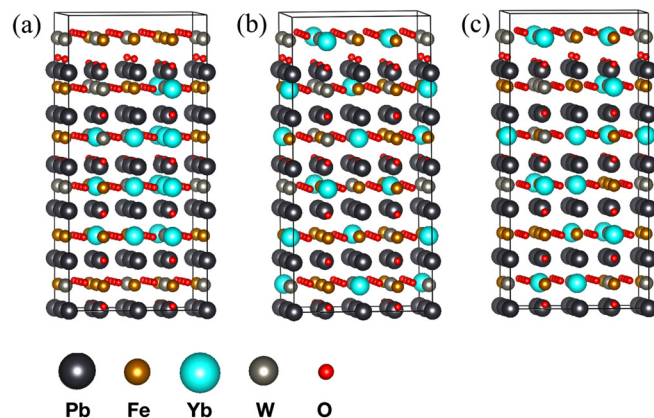


FIG. 5. Structural models with 240 atoms used in the first-principles calculations: (a) clustered, (b) periodic, and (c) random structures of $\text{Pb}(\text{Fe}_{1-x}\text{Yb}_x)_{2/3}\text{W}_{1/3}\text{O}_3$ for $x = 0.375$; structural representations drawn using VESTA.³⁵

TABLE II. The result from calculations with 240 atoms structures, energy difference, unit in meV/atom.

x	Cluster		Periodic		Random	
	AFM	FM	AFM	FM	AFM	FM
0.125	3.71	...	2.38	...	0.00	16.63
0.375	13.33	...	0.00	12.46	9.75	...

Magnetic and dielectric analyses

A sharp kink of the M vs T curve ($H = 100$ Oe) is observed across the Néel temperature $T_N \sim 350$ K for undoped PFWO as shown in the inset of Fig. 7. In the main frame of the figure, the temperature dependence of the magnetization $M(T)$ measured under ZFC and FC conditions at a constant magnetic field $H = 100$ Oe for various Yb doping concentrations ($0.1 \leq x \leq 0.5$) is displayed. All these curves show a sharp upturn across the transition temperature. Below the ordering temperature, all the $M(T)$ curves exhibit irreversibility in ZFC and FC curves suggesting uncompensated magnetic moments at low temperatures. As the Yb doping concentration increases from $x = 0.1$ to 0.5 , the transition temperature T_{mag} decreases from 292 K to 137 K (see Table SM4 in the [supplementary material](#)). The incorporation of Yb inside the PFWO matrix hence alters the magnetic ordering from antiferro to ferrimagnetic leading to the excess/uncompensated moments. For higher doping concentrations $x \geq 0.3$, this sharp upturn becomes less prominent, reflecting the decrease of the magnitude of the excess moment at large x (see below), as well as dilution effects; $x = 0.5$ implies the chemical composition $\text{PbFe}_{1/3}\text{Yb}_{1/3}\text{W}_{1/3}\text{O}_3$, with Fe^{3+} accounting for only one- of the B-site cations.

TABLE III. Average magnetic moments of Fe (Fe and Yb), unit in μ_B .

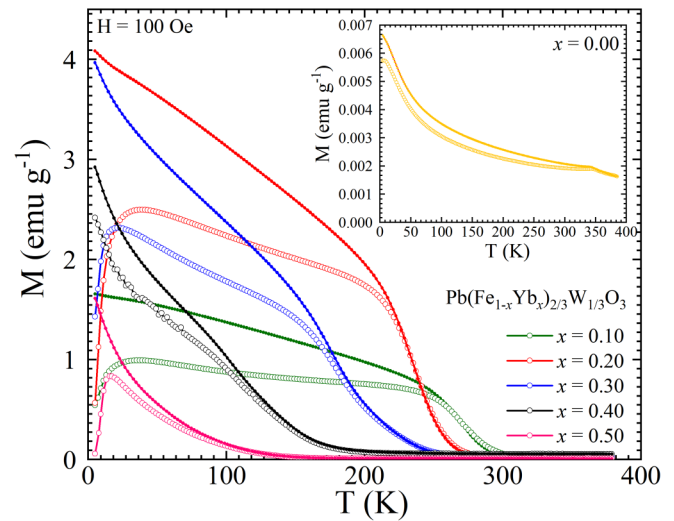
x	Cluster	Periodic	random
0.125	4.17 (3.66)	4.18 (3.67)	4.18 (3.66)
0.250	4.19 (3.15)	4.21 (3.18)	...
0.375	4.18 (2.63)	4.19 (2.64)	4.20 (2.65)

TABLE IV. Average octahedral volume change after doping, unit in \AA^3 .

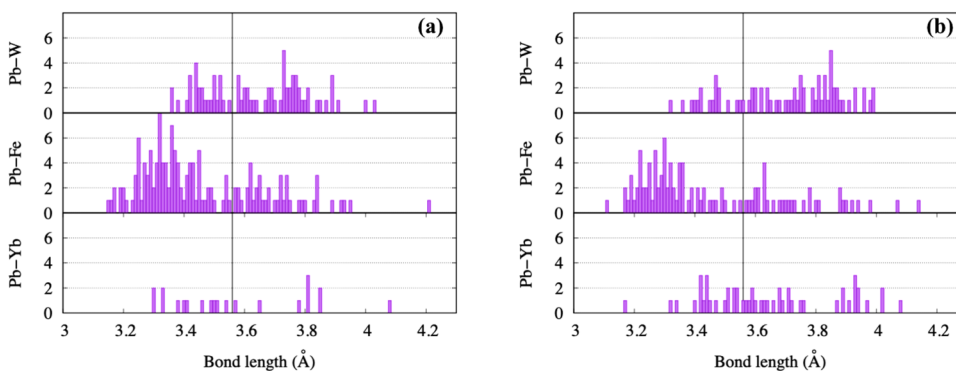
x	WO_6	FeO_6
0.125	0.05	0.25
0.250	0.04	0.20
0.375	0.10	0.20

Figure 8(a) shows the field dependence of magnetization $M(H)$ represented in $\mu_B/\text{f.u.}$ recorded at constant temperature $T = 5 \text{ K}$ for different Yb doping concentrations $0 \leq x \leq 0.5$. The $M(H)$ curves represented in emu/g are shown in Fig. SM3 in the [supplementary material](#). The observed magnetic moments $M(\mu_B/\text{f.u.})$ in all the Yb-doped samples are higher as compared to the undoped PFWO, which is associated with the presence of excess moment caused by unbalanced magnetic sub-lattice. The coercivity of the doped samples, $\sim 200 \text{ Oe}$, may be observed in the inset of Fig. 8(a). Figure 9(a) shows the temperature dependence of dielectric permittivity $\epsilon_r(T)$ at two selected frequencies $f = 2 \text{ kHz}$ and 0.2 MHz , recorded under zero magnetic field for $0 \leq x \leq 0.50$. The corresponding dielectric loss $\tan\delta(T)$ for one selected frequency (2 kHz) is shown in Fig. 9(b). As the temperature increases, ϵ_r increases and attains a maximum across T_m . This peak temperature T_m shifts toward higher temperature ($188 \text{ K} \rightarrow 230 \text{ K}$) with increasing Yb concentration x ($0 \rightarrow 0.50$), while the magnitude of dielectric permittivity decreases ($2911 \rightarrow 497$). The parameters evaluated from the dielectric measurements are listed in Table SM5 in the [supplementary material](#). At higher temperatures ($T > 250 \text{ K}$), the much higher dielectric permittivity of undoped PFWO is likely associated with the presence of oxygen vacancies or Pb vacancies.^{21,22} The frequency dispersion of the high temperature dielectric permittivity was fitted to the Debye relaxation model (Arrhenius law).²² The effect of oxygen vacancies on $\epsilon_r(T)$ and $\tan\delta(T)$ for $x = 0.1$ is discussed in Ref. 21. The contribution of oxygen vacancies seems to be less effective with increasing Yb concentration.

Another important characteristic observed from Fig. 9(a) is the frequency dispersion of the dielectric maximum $\epsilon_r(T_m)$. In order to observe the frequency dispersion, the $\epsilon_r(T)$ and $\tan\delta(T)$ data for $x = 0.2$ are shown for various frequencies $200 \text{ Hz} \leq f \leq 2 \text{ MHz}$ in Figs. 10(a) and 10(b), respectively. The frequency dependence of T_m

**FIG. 7.** Temperature dependence of magnetization $M(T)$ measured under ZFC (open symbols) and FC (filled symbols) conditions at a constant magnetic field $H = 100 \text{ Oe}$ for various Yb doping concentrations ($0.1 \leq x \leq 0.5$). The inset shows the corresponding curve for $x = 0$.

follows the Vogel–Fulcher (VF) law [the inset of Fig. 10(a)] as given by $\tau = \tau_0 \exp \left[\frac{E_a}{k_B(T_m - T_{VF})} \right]$, where E_a ($= 0.12 \text{ eV}$) is the activation energy, T_{VF} ($= 159 \text{ K}$) is the freezing temperature of the polarization function, k_B is the Boltzmann constant, and the pre-exponential factor τ_0 ($= 2.2 \times 10^{-13} \text{ s}$) is known as the characteristic relaxation time (Ref. 21 and references therein). For other compositions, these parameters are listed in Table SM5 in the [supplementary material](#). The observed value of τ_0 decreases with increasing x , while the activation energy E_a increases. For compositions $x = 0, 0.1$, and 0.2 , these values are in good agreement with lead magnesium niobate ($\tau_0 = 1.54 \times 10^{-13} \text{ s}$ and $E_a = 0.04 \text{ eV}$), which is an example of a classical relaxor ferroelectric.¹⁹ It is also reported in Ref. 21 that the dielectric properties of the $x = 0.1$ sample shows an unusual re-entrant ferroelectric relaxor behavior with a ferroelectric like transition at 280 K and a re-entrant relaxor behavior around 190 K .

**FIG. 6.** Pb–B bond length distribution of the ground state structure in 240 atoms structural model: (a) $x = 0.125$ and (b) $x = 0.375$. The vertical line is the average Pb–B bond length.

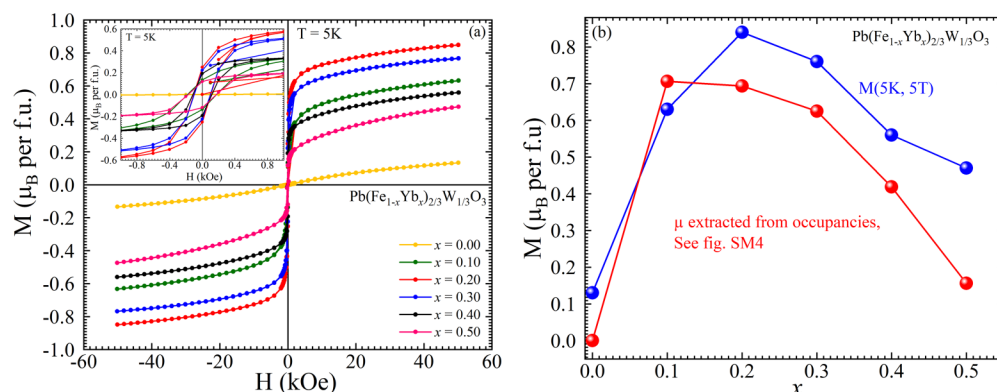


FIG. 8. (a) Magnetic field dependence of magnetization $M(H)$ represented in $\mu_B/\text{f.u.}$ recorded at constant temperature $T = 5$ K for different Yb doping concentrations $0 \leq x \leq 0.5$. The inset shows a zoomed view of the main panel; see Fig. SM3 in the [supplementary material](#) for the magnetization data in emu/g. (b) The compositional dependence of $M(\mu_B/\text{f.u.})$ at $T = 5$ K and $H = 5$ T (blue color), and excess moment extracted from the Fe occupancies $[(\text{Fe}(4a) - \text{Fe}(4b)) \times 5\mu_B] \times 1/2$ is shown using the red color circular symbols (see the main text and Figs. SM4 and SM5 in the [supplementary material](#) for details).

DISCUSSION

The obtained XRPD patterns indicate that all PFYWO samples adopt a cubic ($Fm\bar{3}m$) structure. Above $x = 0.5$, it was impossible to prepare single phase samples with the perovskite structure. The first-principles calculations support the stabilization of the ordered phase by Yb substitution. However, the real structural mechanism of the ordering transformation in PFYWO remains unknown and important factors in triggering the $Pm\bar{3}m \rightarrow Fm\bar{3}m$ transformation are still not fully clear.^{18,38}

In ordered PFYWO perovskites, the $B(4b)$ position is occupied by a larger ferroelectrically “inactive” cation (Yb^{3+}) and the $B(4a)$ position by a smaller ferroelectrically “active” cation (W^{6+}) and the intermediate oxygen anions will be displaced toward the $B(4a)$ position. This anion displacement probably induces movement of the Pb cation along $\langle 111 \rangle$ toward the $B(4b)$ position in order to accommodate the lone pair of electrons of Pb^{2+} cations. This cooperative displacement mechanism can then provide for extended ferroelectric coupling. The length of ferroelectric correlations in $B(4a)$ position could be tailored by controlling the concentration of the

ferroelectrically active W^{6+} cations. Because of the overall 2:1 B -site chemistry in PFWO-type perovskites, the degree of chemical disorder plays a central role in frustrating long-range ferroelectric coupling. Following conclusions made in Refs. 39 and 40, we can suggest that both normal ferroelectric and relaxor ferroelectric have the same polarization mechanism, i.e., inherent correlated cation and neighboring O anion displacements forming dipole clusters [or polar nano regions (PNR)]. The role of the substituting ions is not to induce the PNR's but rather to suppress homogeneous strain distortion, transverse correlation of PNR's, and a transition into a long-range ordered ferroelectric state. A possible reason for the onset of ferroelectricity for $x = 0.1$ could hence be related to the remarkable increase in the concentration of ferroelectric-active W^{6+} cations at the $B(4a)$ position observed in Fig. 4 for that composition in addition to the cationic ordering.

The abnormally large atomic displacement parameters for Pb cations (thermal parameter $B_{\text{Pb}} = 3.7 \text{ \AA}^2$) provide strong evidence for the presence of disordered atomic displacements. Such behavior is typical for Pb-based perovskites containing Pb^{2+} on the A-site due to the presence of a stereo active electron lone pair on

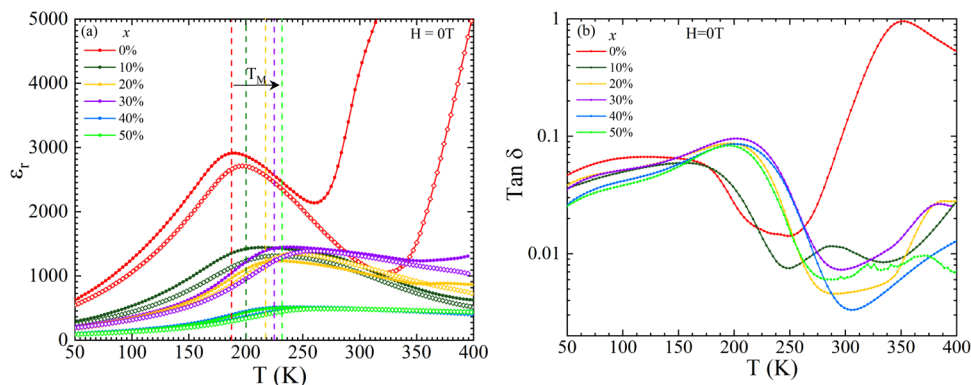


FIG. 9. Temperature dependence of (a) dielectric permittivity $\epsilon_r(T)$ at two selected frequencies $f = 2$ kHz (filled symbols) and 0.2 MHz (open symbols) and (b) dielectric loss $\tan\delta(T)$ for a selected frequency ($f = 2$ kHz) recorded under zero magnetic field for $0 \leq x \leq 0.5$.

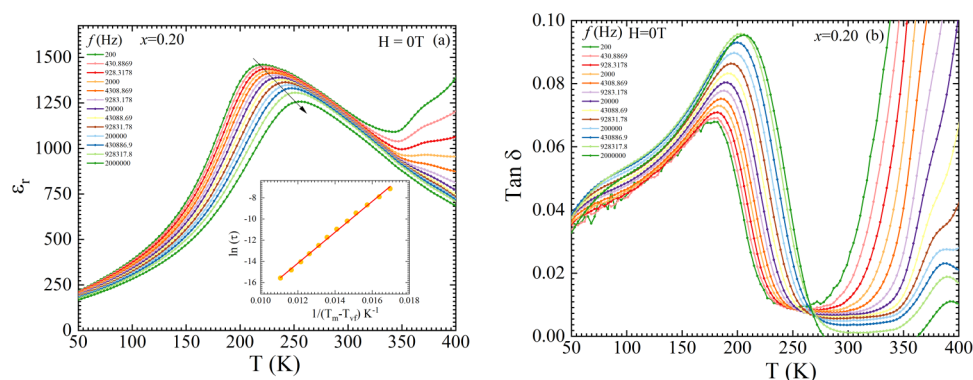


FIG. 10. Temperature dependence of (a) $\epsilon_r(T)$ and (b) $\tan\delta(T)$ recorded at various frequencies ($200 \text{ Hz} \leq f \leq 2 \text{ MHz}$) for $x=0.2$. The circular symbols in the inset of (a) show the logarithmic variation of τ as a function of $1/(T_m - T_{VF})$ and the solid continuous line is the best-fit to the Vogel-Fulcher equation.

Pb^{2+} cations.⁴¹ Although a Pb deficiency appears unlikely because of the preparation method, the Pb stoichiometry was tested by refining its occupancy factor. The refined value indicated full site occupancy with an unchanged value of B_{pb} . Therefore, the meaning of such a large Pb displacement parameter has been examined. It is known^{41,42} that improvements can be obtained by considering Pb located in a multi-minimum potential around its Wyckoff position. We have attempted to model these displacements by moving the Pb^{2+} cation away from the high-symmetry site in a disordered fashion. We have tested the three kinds of Pb disorder, i.e., along $\langle 100 \rangle$, $\langle 110 \rangle$, and $\langle 111 \rangle$ directions. The difference between these models is not very pronounced (the reliable factors, R_B are 2.73%, 2.54%, and 2.23%, respectively). The magnitude of the displacement of the Pb cation from its high-symmetry position is around $0.25(2) \text{ \AA}$ independent of Yb concentration and the observed short-range Pb^{2+} displacements appear randomly distributed, mostly displaced along $\langle 111 \rangle$. This displacement can be explained as a consequence of the repulsion between the non-bonded 6s lone electron pair of Pb and the Pb–O bonds of its own coordination polyhedron, supposing that the lone pair is directed toward one of the vertices of the cube. The Pb shift along the $\langle 111 \rangle$ direction increases slightly the angles between the lone pair and all the Pb–O bonds, minimizing the repulsion effects. It was established that for Pb cation coordinated to 12 oxygen anions, there exist only two crystallographic directions, $[100]$ and $[111]$, along which the non-bonded pair can be directed.⁴³

In an earlier study of Sc doped PFWO (PFSWO) investigated by both XRPD and NPD,¹⁸ whose data were jointly refined to determine occupancies with great accuracy. We have observed a good match between the values of the magnetic moments determined from NPD and those obtained by the simple multiplication of the determined Fe occupancies by $5\mu_B$ (the expected moment value for Fe^{3+}), which we denote “ $\mu(\text{Fe-occupancies} \times 5\mu_B)$ ” (see Fig. SM4 in the [supplementary material](#), data obtained from Ref. 18). We hence use the occupancies from XRPD data to predict the respective magnetic moments (occupancies $\times 5\mu_B$) in PFYWO. Figure SM5 in the [supplementary material](#) shows the compositional dependence of B-site magnetic moment evaluated using the Fe-occupancies determined from the XRPD data (Fe-occupancies $\times 5\mu_B$). The blue color and red color solid symbols show the 4b and 4a-site moment, respectively. The black

color dashed line represents the average moment determined by the formula $[2/3 \times (1-x) \times 5\mu_B]$, which is consistent with the average of 4a and 4b-site moment (solid symbols). The difference in 4a and 4b-site moment is shown using hollow symbols. The compositional dependence of $M(\mu_B/\text{f.u.})$ at $T = 5 \text{ K}$ and $H = 5 \text{ T}$ is shown in Fig. 8(b) (blue color). The value of $M(\mu_B/\text{f.u.})$ increases initially with increasing x ; after a certain composition $x > 0.2$, the $M(\mu_B/\text{f.u.})$ decreases continuously. As shown in Fig. 8(b), this behavior is consistent with the moment extracted from the Fe-occupancies shown by the red color circular symbols.

As compared to PFSWO where the cationic order is strongly dependent on heat treatments,¹⁸ the magnetic properties and phase stability of PFYWO remain independent of such effects. The comparison of magnetic properties between quenched and slowly cooled samples is shown in Fig. SM6 in the [supplementary material](#). The magnetic properties of these differently synthesized samples are almost identical indicating ordered PFYWO samples without any special heat treatment.

Although several relaxation mechanisms have been proposed in the literature (see details in Ref. 44), it is still rather difficult to identify the origin of the relaxor behavior in these systems, which stems from the local nanoscale crystal structure ordering and associated structural relaxation as well as inherent displacive cation disorder. The dielectric data from Fig. 9(a) are plotted in Fig. 11 as the temperature dependence of normalized dielectric permittivity $\epsilon_r/\epsilon_r(T_m)$ for a selected frequency $f = 0.02 \text{ MHz}$ under zero magnetic field. Between the two extreme compositions, $x = 0.1$ appears as a boundary composition below and above which the dielectric behavior appears differently. The transition from a single dielectric peak to a twin peak was noticed from $x = 0$ to $x = 0.1$. For $x = 0.1$, the first peak at 192 K ($f = 1 \text{ kHz}$) shows a frequency dispersion and the second peak observed at 280 K is frequency independent, suggesting a re-entrant ferroelectric behavior.²¹ This temperature is in the vicinity of T_{mag} .²¹ Below $x \leq 0.1$, all samples exhibit magnetic field dependence where the magnitude of ϵ_r decreases with the application of the magnetic field. A similar H dependence is observed for $x = 0.2$, whereas for samples with $x > 0.2$, ϵ_r is independent of the superimposed magnetic field. The magnetic field dependence ϵ_r and $\tan\delta$ of two compositions $x = 0.2$ and 0.3 are shown in Fig. SM7 in the [supplementary material](#). Data for the $x = 0.4$ and 0.5 compositions are also added in Fig. SM8 in the

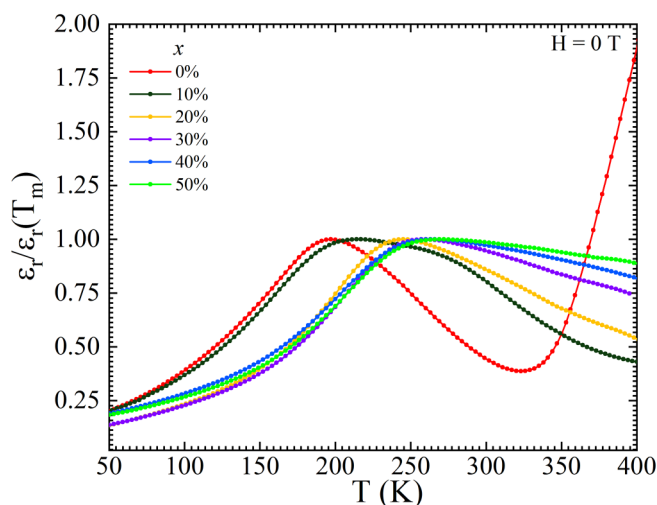


FIG. 11. Temperature dependence of the normalized dielectric permittivity $\epsilon_r/\epsilon_r(T_m)$ for a selected frequency $f = 0.02$ MHz under zero magnetic field.

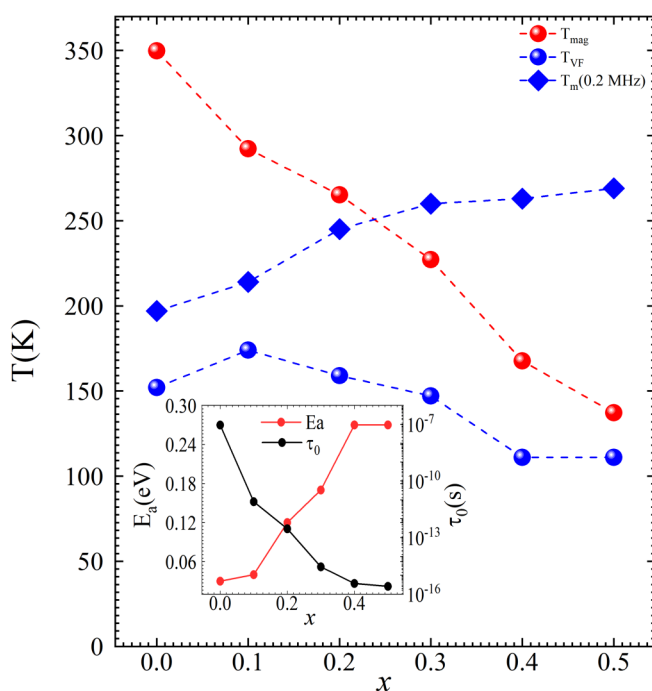


FIG. 12. Electronic phase diagram for the $\text{Pb}(\text{Fe}_{1-x}\text{Yb}_x)_{2/3}\text{W}_{1/3}\text{O}_3$ series: compositional dependence of the temperature onset of (ferri)magnetic order (T_{mag}), temperature of maximum of dielectric anomaly T_m at $f = 0.2$ MHz, and dielectric freezing temperature (T_{VF}) obtained from the Volger–Fulcher analysis. The inset shows the corresponding activation energy (E_a) and pre-exponential factor (τ_0).

[supplementary material](#) for completeness. The evolution of the magnetic and dielectric properties of the system upon doping is summarized in the electronic phase diagram depicted in [Fig. 12](#). The magnetic ordering temperature T_{mag} monotonously decreases as x increases, while T_m , characteristic of the ferroelectric relaxor behavior, slightly increases. The parameters extracted from the Volger–Fulcher analysis of the dielectric data are also included in the main frame and the inset of [Fig. 12](#). While T_{VF} shows a relatively mild variation with the Yb content, the activation energy E_a was found to increase by nearly an order of magnitude as x increases, τ_0 decreasing by several orders of magnitude (see Table SM5 in the [supplementary material](#) for numerical values).

CONCLUSIONS

Structural, magnetic, and dielectric properties of stoichiometric and single phased $\text{Pb}(\text{Fe}_{1-x}\text{Yb}_x)_{2/3}\text{W}_{1/3}\text{O}_3$ ($0 \leq x \leq 0.5$) ceramics have been investigated. Cationic order was observed over the full concentration range of Yb substitution ($0.1 \leq x \leq 0.5$). In this “random site” structure, one position is occupied solely by $\text{Fe}(\text{Yb})$, but the other contains a random mixture of W and the remaining $\text{Fe}(\text{Yb})$ cations. The ordering of the structure is supported by results from first-principles electronic structure calculations. It is interesting to note that the effect of Yb and Sc substituents within concentration range up to 50% on the ordering in PFWO is very similar. As a result of the ordering and unbalanced occupancies of the magnetic Fe^{3+} cations on the B-sites of the ordered structure, the antiferromagnetic state of the undoped compound is switched to a ferrimagnetic state with substantial magnitude of the excess moment. Our results also show that Yb doping induces significant changes of the dielectric properties of PFWO, particularly in the low doping ($x \sim 0.1$) region where re-entrant ferroelectric-like behavior is observed.

SUPPLEMENTARY MATERIAL

See the [supplementary material](#) for experimental details concerning the synthesis and analysis of the materials, and additional tables and figures. The tables list the results of the analysis of the composition (EDS), structural, magnetic, and dielectric properties of the materials. The figures illustrate the microstructure (SEM images) and give more details on the magnetic and dielectric properties of the compounds.

ACKNOWLEDGMENTS

We thank the Stiftelsen Olle Engkvist Byggmästare, the Swedish Research Council (VR), and Russian Foundation for Basic Research (No. 18-03-00245) for financially supporting this work. We thank Pedro Berastegui, Uppsala University, for his expert help. D.W. acknowledges the China Scholarship Council (Grant No. 201706210084) for financial support. D.W. and B.S. acknowledge SNIC-UPPMAX, SNIC-HPC2N, and SNIC-NSC centers under the Swedish National Infrastructure for Computing (SNIC) resources for the allocation of time in high-performance supercomputers. Moreover, supercomputing resources from PRACE DECI-15 project DYNAMAT are gratefully acknowledged.

DATA AVAILABILITY

The data that support the findings of this study are available from the corresponding author upon reasonable request.

REFERENCES

- ¹N. A. Spaldin and R. Ramesh, *Nat. Mater.* **18**, 203 (2019).
- ²J. Varignon, N. C. Bristowe, E. Bousquet, and P. Ghosez, *Phys. Sci. Rev.* **5**, 20190069 (2020).
- ³S. Krohns and P. Lunkenheimer, *Phys. Sci. Rev.* **4**, 20190015 (2019).
- ⁴H. Palneedi, V. Annappureddy, S. Priya, and J. Ryu, *Actuators* **5**, 9 (2016).
- ⁵B. Wang, "Multiferroic materials," in *Mechanics of Advanced Functional Materials, in Advanced Topics in Science and Technology in China* (Springer, Berlin, 2013).
- ⁶M. M. Vopson, *Crit. Rev. Solid State Mater. Sci.* **40**, 223 (2015).
- ⁷K. F. Wang, J.-M. Liu, and Z. F. Ren, *Adv. Phys.* **58**, 321 (2009).
- ⁸P. Juhas, I. Grinberg, A. M. Rappe, W. Dmowski, T. Egami, and P. K. Davies, *Phys. Rev. B* **69**, 214101 (2004).
- ⁹P. Juhas, P. K. Davies, and M. A. Akbas, *AIP Conf. Proc.* **626**, 108 (2002).
- ¹⁰P. Juhas, P. K. Davies, and M. A. Akbas, *J. Am. Ceram. Soc.* **87**, 2086 (2004).
- ¹¹G. King and P. M. Woodward, *J. Mater. Chem.* **20**, 5785 (2010).
- ¹²V. A. Isupov, *Ferroelectrics* **315**, 149 (2005).
- ¹³G. A. Smolenski, A. I. Agranovskaya, and V. A. Isupov, *Sov. Phys. Solid State* **1**, 907 (1959).
- ¹⁴G. A. Smolenskii, *J. Phys. Soc. Jpn.* **28**, 26 (1970).
- ¹⁵L. Zhou, P. M. Vilarinho, P. Q. Mantas, J. L. Baptista, and E. Fortunato, *J. Eur. Ceram. Soc.* **20**, 1035 (2000).
- ¹⁶S. A. Ivanov, "Magnetoelectric complex metal oxides main features of preparation, structure and properties," in *Advanced Functional Materials, Volume 2*, edited by B. Sanyal and O. Eriksson (Elsevier, Oxford, 2012), pp. 163–234.
- ¹⁷R. N. P. Choudhary, D. K. Pradhan, C. M. Tirado, G. E. Bonilla, and R. S. Katiyar, *Phys. Status Solidi (B)* **244**, 2254 (2007).
- ¹⁸S. A. Ivanov, P. Beran, A. A. Bush, T. Sarkar, S. Shafeie, D. Wang, B. Sanyal, O. Eriksson, M. Sahlberg, Y. Kvashnin, R. Tellgren, P. Nordblad, and R. Mathieu, *Eur. Phys. J. B* **92**, 163 (2019).
- ¹⁹L. Zhou, P. M. Vilarinho, and J. L. Baptista, *J. Appl. Phys.* **85**, 2312 (1999).
- ²⁰D. Brzezinska, R. Skulski, D. Bochenek, P. Niemiec, A. Chrobak, L. Fajfrowski, and S. Matyjasik, *J. Alloys Compd.* **737**, 299 (2018).
- ²¹D. C. Joshi, S. A. Ivanov, A. A. Bush, T. Sarkar, Z.-G. Ye, P. Nordblad, and R. Mathieu, *Appl. Phys. Lett.* **115**, 072902 (2019).
- ²²S. A. Ivanov, A. A. Bush, C. Ritter, M. A. Behtin, V. M. Cherepanov, C. Autieri, Y. O. Kvashnin, I. Di Marco, B. Sanyal, O. Eriksson, P. Anil Kumar, P. Nordblad, and R. Mathieu, *Mater. Chem. Phys.* **187**, 218 (2017).
- ²³S. Matteppanavar, S. Rayaprol, B. Angadi, and B. Sahoo, *J. Supercond. Nov. Magn.* **30**, 1317 (2017).
- ²⁴Z. G. Ye, K. Toda, and M. Sato, *J. Korean Phys. Soc.* **32**, S1028 (1998).
- ²⁵S. A. Ivanov, S.-G. Eriksson, R. Tellgren, and H. Rundlof, *Mater. Res. Bull.* **39**, 2317 (2004).
- ²⁶B. Fraygola, A. Mesquita, A. A. Coelho, D. Garcia, V. R. Mastelaro, and J. A. Eiras, *Phys. Status Solidi (A)* **210**, 386 (2013).
- ²⁷Z.-G. Ye and H. Schmid, *J. Cryst. Growth* **167**, 628 (1996).
- ²⁸J. Rodriguez-Carvajal, *Phys. B Condens. Matter* **192**, 55 (1993).
- ²⁹G. Kresse and J. Furthmüller, *Phys. Rev. B* **54**, 11169 (1996).
- ³⁰G. Kresse and D. Joubert, *Phys. Rev. B* **59**, 1758 (1999).
- ³¹J. P. Perdew, K. Burke, and M. Ernzerhof, *Phys. Rev. Lett.* **77**, 3865 (1996).
- ³²A. I. Lichtenstein, V. I. Anisimov, and J. Zaanen, *Phys. Rev. B* **52**, R5467 (1995).
- ³³V. I. Anisimov, F. Aryasetiawan, and A. I. Lichtenstein, *J. Phys. Condens. Matter* **9**, 767 (1997).
- ³⁴G. Rollmann, A. Rohrbach, P. Entel, and J. Hafner, *Phys. Rev. B* **69**, 165107 (2004).
- ³⁵K. Momma and F. Izumi, "VESTA 3 for three-dimensional visualization of crystal, volumetric and morphology data," *J. Appl. Crystallogr.* **44**, 1272 (2011).
- ³⁶R. D. Shannon, *Acta Crystallogr. A* **32**, 751 (1976).
- ³⁷J. Blasco, C. Ritter, L. Morellon, P. A. Algarabel, J. M. De Teresa, D. Serrate, J. García, and M. R. Ibarra, *Solid State Sci.* **4**, 651 (2002).
- ³⁸K. S. Aleksandrov, S. V. Misyul, and E. E. Baturinets, *Ferroelectrics* **354**, 60 (2007).
- ³⁹L. E. Cross, *Ferroelectrics* **76**, 241 (1987).
- ⁴⁰A. A. Bokov and Z.-G. Ye, *J. Mater. Sci.* **41**, 31 (2006).
- ⁴¹S. A. Larregola, J. A. Alonso, M. Alguero, R. Jimenez, E. Suard, F. Porcher, and J. C. Pedregosa, *Dalton Trans.* **39**, 5159 (2010).
- ⁴²C. Malibert, M. Dkhil, M. Dunlop, J. M. Kiat, G. Baldinozzi, and S. B. Vakhrushev, *Ferroelectrics* **235**, 87 (1999).
- ⁴³J. A. Alonso and I. Rasines, *J. Phys. Chem. Solids* **49**, 385 (1988).
- ⁴⁴L. Chen, A. A. Bokov, W. Zhu, H. Wu, J. Zhuang, and Z. G. Ye, *Sci. Rep.* **6**, 22327 (2016).